



OPEN ACCESS

EDITED BY
Rhea Coler,
University of Washington, United States

REVIEWED BY
Kathirvel Maruthai,
Johns Hopkins University, United States
Mohd Saqib,
Albany Medical College, United States

*CORRESPONDENCE
Brendan K. Podell
✉ bpodell@colostate.edu

†These authors share senior authorship

RECEIVED 03 May 2024
ACCEPTED 23 July 2024
PUBLISHED 26 August 2024

CITATION
Cooper SK, Ackart DF, Lanni F,
Henao-Tamayo M, Anderson GB and
Podell BK (2024) Heterogeneity in immune
cell composition is associated with
Mycobacterium tuberculosis replication
at the granuloma level.
Front. Immunol. 15:1427472.
doi: 10.3389/fimmu.2024.1427472

COPYRIGHT
© 2024 Cooper, Ackart, Lanni, Henao-Tamayo,
Anderson and Podell. This is an open-access
article distributed under the terms of the
[Creative Commons Attribution License \(CC BY\)](https://creativecommons.org/licenses/by/4.0/).
The use, distribution or reproduction in other
forums is permitted, provided the original
author(s) and the copyright owner(s) are
credited and that the original publication in
this journal is cited, in accordance with
accepted academic practice. No use,
distribution or reproduction is permitted
which does not comply with these terms.

Heterogeneity in immune cell composition is associated with *Mycobacterium tuberculosis* replication at the granuloma level

Sarah K. Cooper^{1,2}, David Forrest Ackart^{1,2}, Faye Lanni^{1,2},
Marcela Henao-Tamayo^{1,2}, G. Brooke Anderson^{2,3†}
and Brendan K. Podell^{1,2,4*†}

¹Mycobacteria Research Laboratories, Department of Microbiology, Immunology, and Pathology, Colorado State University, Fort Collins, CO, United States, ²Phoenix Immune Mechanisms of Protection Against Tuberculosis Center, Seattle, WA, United States, ³Department of Environmental and Radiological Health Sciences, Colorado State University, Fort Collins, CO, United States, ⁴Consortium for Applied Microbial Metrics, Aurora, CO, United States

The control of bacterial growth is key to the prevention and treatment of tuberculosis (TB). Granulomas represent independent foci of the host immune response that present heterogeneous capacity for control of bacterial growth. At the whole tissue level, B cells and CD4 or CD8 T cells have an established role in immune protection against TB. Immune cells interact within each granuloma response, but the impact of granuloma immune composition on bacterial replication remains unknown. Here we investigate the associations between immune cell composition, including B cell, CD4, and CD8 T cells, and the state of replicating *Mycobacterium tuberculosis* (*Mtb*) within the granuloma. A measure of ribosomal RNA synthesis, the RS ratio®, represents a proxy measure of *Mtb* replication at the whole tissue level. We adapted the RS ratio through use of *in situ* hybridization, to identify replicating and non-replicating *Mtb* within each designated granuloma. We applied a regression model to characterize the associations between immune cell populations and the state of *Mtb* replication within each respective granuloma. In the evaluation of nearly 200 granulomas, we identified heterogeneity in both immune cell composition and proportion of replicating bacteria. We found clear evidence of directional associations between immune cell composition and replicating *Mtb*. Controlling for vaccination status and endpoint post-infection, granulomas with lower CD4 or higher CD8 cell counts are associated with a higher percent of replicating *Mtb*. Conversely, changes in B cell proportions were associated with little change in *Mtb* replication. This study establishes heterogeneity across granulomas, demonstrating that certain immune cell types are differentially associated with control of *Mtb* replication. These data suggest that evaluation at the granuloma level may be imperative to identifying correlates of immune protection.

KEYWORDS

Mycobacterium tuberculosis, granuloma, immunohistochemistry (IHC), *in situ* hybridization (ISH), image analysis

1 Introduction

Tuberculosis (TB) granulomas are isolated and multifocal structures formed by the host immune response to combat *Mycobacterium tuberculosis* (*Mtb*) infection. Their role is to contain and clear the bacteria, thereby preventing further bacterial replication, disease, and transmission. However, granuloma formation plays contradictory roles in TB disease; while the formation of granulomas control *Mtb* replication, they also allow *Mtb* to persist and replicate (1). There is considerable heterogeneity in the pathology, immune cell composition and structure of granulomas (2, 3). The underlying immune mechanisms that contribute to control of *Mtb* infection across the heterogeneous population of granulomas are poorly understood. Determining natural and vaccine-mediated immune protection at the granuloma level can provide key insights into developing more effective vaccines and therapeutics.

Heterogeneity has been described in granulomas across multiple species including human, non-human primate (NHP), rabbit, guinea pig, and some strains of mice. Granulomas within the same host may appear simultaneously active and inactive by PET-CT imaging in both humans and non-human primate (NHP) models (4–6). Autopsies of human subjects show a wide diversity in granuloma morphology across disease states (7, 8), which is also reflected by NHP models (9). Some NHP granulomas demonstrate evidence of resolution by histopathology and PET-CT imaging, while others in the same host, remain active (10). While substantial heterogeneity exists across many of commonly used mouse strains (11–13), the guinea pig as a small rodent model uniquely demonstrates central caseous necrosis and granuloma organization that is characteristic of human TB (14–16). When evaluated in individual granulomas, the culturable bacterial burden used to assess protection has revealed a wide range of heterogeneity consistent with these pathology observations (17). Collectively, evidence across multiple model species and human subjects supports the presence of substantial heterogeneity in granuloma composition and function.

CD4 T cells represent the cornerstone of antimycobacterial immunity. Murine studies eliminating CD4 T cells from the immune response have demonstrated loss of protection, based on changes in culturable burden from infected lung tissue (18, 19). This protection includes both IFN γ dependent and independent mechanisms derived from CD4 T cells (18). These CD4 T cells are present in multiple states of differentiation, polarization, effector functions or memory phenotypes (20, 21). Recently, a role for B cell derived antibody and CD8 T cells has been shown in correlates of immune protection (22). Antigen-specific antibodies may exert multiple effector functions in response to *Mtb* infection including antibody-dependent cellular cytotoxicity, opsonization and facilitated phagocytosis, as well as fixation and activation of complement (23, 24). Although functions of CD8 T cells are less understood, these cells are critical to control of TB progression with links to granzymes and cytotoxic function (25–27). Although important to immune protection, the contribution of these adaptive immune cell types to granuloma success or failure

remains poorly understood, primarily due to limited methods that simultaneously measure both host cell populations and individual bacterial response within a single granuloma.

Protection is typically determined by measuring differences in culturable *Mtb* from tissue via colony forming units (CFU). Although this offers important information on bacterial burden, it only measures *Mtb* capable of growth on solid agar and as such cannot provide a specific location from where the bacteria were derived. Location is particularly important in considering granuloma heterogeneity because granulomas within a single animal may exist in differing states or have differing degrees of capacity for bacterial control. Previously, observation of *Mtb* in granulomas of pathology specimens has been limited to use of either reporter strains, or cell-wall based staining through IHC or variations on the traditional acid-fast stain. These methods have limitations in both stability and reproducibility, as well as capacity to detect the total *Mtb* population (28–30). These measures also fail to provide information on the physiologic status or replicative response of the *Mtb* bacilli.

A novel adjunctive measure to CFU, the RS ratio[®], measures the ratio of *Mtb* immature pre-rRNA relative to mature 23S rRNA, representing ongoing rRNA synthesis (31). We have previously shown that the RS ratio effectively serves as a proxy measure of bacterial replication status. By applying *in situ* hybridization (ISH) probes targeting these regions of rRNA, we have established the RS ratio ISH approach for detection of *Mtb* bacilli and their state of replication, thereby enabling investigation of both the host and pathogen response within a single granuloma. This approach can measure changes in response over time, and in response to vaccination, across states of both host cell populations and *Mtb* replication. Here, we measure CD4 T cell, CD8 T cell, and B cell populations using multiplexed fluorescent IHC simultaneously with the RS ratio ISH across granulomas of unvaccinated and BCG-vaccinated mice, demonstrating an association between granuloma immune cell composition and *Mtb* replication rates.

The heterogeneous nature of immune cell composition across granulomas, as demonstrated by this study, provides strong evidence that certain immune cells have a greater influence on the control of *Mtb* replication. These results emphasize the need for granuloma-focused investigations to advance the understanding of protective immunity against *Mtb* infection and inform novel vaccine and therapeutic strategies.

2 Materials and methods

2.1 Animals

Male and female C57BL/6 mice, 4–6 weeks of age, were purchased from The Jackson Laboratory. Mice were housed in a biosafety level 3 animal facility at Colorado State University (CSU), and all experimental protocols and procedures were performed in accordance with the CSU Institutional Animal Care and Use Committee under protocol number 1278. Mice were euthanized by CO₂ inhalation at 56 or 114 days after exposure to *Mtb*.

2.2 Vaccination

Mice were mock-vaccinated with 50 μ l of phosphate buffered saline (PBS) or vaccinated with the human clinical-grade Danish-1331 BCG vaccine, Lot #120005-C (AJ Vaccines), by intradermal injection at the tail base. Assuming a stock bacterial concentration of 2×10^6 BCG organism per ml, as provided by the manufacturer, a targeted dose of 1×10^4 CFU was administered in a 50 μ l injection volume to each mouse.

2.3 *Mycobacterium tuberculosis* infection

150 days post-vaccination with BCG, mice were infected by low-dose aerosol with *Mtb* Erdman (BEI Resources) using a Glas-Col aerosol chamber targeting an exposure dose of 50–100 CFU, as previously described (32). Immediately post-exposure, three mice were euthanized and whole lung homogenate was plated on 7H11 agar plates to confirm aerosol delivery of expected exposure dose, achieving a mean exposure dose of 54 CFU per mouse.

2.4 Bacterial enumeration by CFU

At necropsy, the right caudal lung lobe of each mouse was collected and homogenized in PBS using a Bullet Blender Blue (Next Advance) device at speed 8 setting for 4 minutes, as previously described (33). Tissue homogenate was plated at serial 1:5 dilutions on 7H11 agar plates and final CFU counts were enumerated following 8 weeks of incubation.

2.5 Histopathology and image analysis

One third of the left lung lobe was collected at necropsy and immediately fixed in 4% paraformaldehyde for 48 hours before being paraffin embedded. 5 μ m tissue sections were cut and mounted on charged microscope slides, stained with hematoxylin and eosin (H&E), and scanned at 20X magnification using an Olympus VS120 scanning microscope, Hamamatsu ORCA-R2 camera, and Olympus VS-ASW 2.9 software available through the Experimental Pathology Facility at Colorado State University.

Visiopharm software was used for image analysis. Entire lung section regions of interest (ROI) were identified at 5X magnification with a custom algorithm that utilizes decision forest training to differentiate tissue from microscope slide based on color and area. An additional custom-made algorithm based on decision forest training and classification based on staining intensity, area, and morphological features at 20X magnification was created to automate granuloma detection. A final algorithm was used for quantification of area of both granulomas and healthy tissue within tissue section ROIs to calculate percent granuloma lesion burden. Identified granulomas and calculations received a final review by a pathologist (Podell BK) (34).

2.6 Multiplex fluorescent immunohistochemistry

Slides were deparaffinized and stained using a Leica Bond RXm automated slide stainer and associated Leica Bond reagents (Supplementary Table 1). Heat induced epitope retrieval (HIER) was performed on tissues with ER1 solution at 97°C for 30 minutes prior to quenching endogenous peroxidase activity with 3% hydrogen peroxide. Tissues were blocked using 2.5% Normal Goat Serum Blocking Solution (Vector Laboratories) then incubated with the following rat monoclonal primary antibodies: CD4 (1:100, clone 4SM95, catalog number 14-9766-82, eBioscience), CD8a (1:100, clone 4SM15, catalog number 14-0808-82, eBioscience), and CD45R/B220 (1:100, clone RA3-6B2, catalog number 103201 BD Biosciences). Sections were incubated with undiluted ImmPRESS mouse adsorbed goat anti-rat IgG-HRP polymer (Vector Laboratories) for primary antibody detection. Visualization of cell surface markers was accomplished using Opal 520 (1:200), Opal 570 (1:200), and TSA plus Cyanine 5 (1:1000) in 1X TSA Plus Automation Amplification Diluent (Akoya Biosciences). Antibody stripping was performed using HIER at 95°C and ER1 solution for 20 minutes (Leica Biosystems) between each antibody application in the following order: CD4 detected with Opal 520, CD8 detected with Opal 570, and B220 detected with Cyanine 5. Finally, nuclei were stained with Spectral DAPI (Akoya Biosciences). Whole stained lung sections were scanned at 20X magnification using an Olympus VS120 microscope, Hamamatsu ORCA-R2 camera, and Olympus VS-ASW 2.9 software at the Experimental Pathology Facility at Colorado State University. Exposure times were determined using the autoexposure function and adjusted to distinguish antibody detection of cell surface markers from erythrocyte background.

2.7 Multiplex fluorescent *in situ* hybridization

Slides cut in serial to those used for multiplex IHC were deparaffinized and targets hybridized using the RNAscope LS multiplex fluorescent reagents (Advanced Cell Diagnostics) according to the manufacturer's recommendations for use on the Leica Bond RXm automated slide stainer and respective Leica Bond reagents (Supplementary Table 1). HIER was performed on tissues with ER2 solution (Leica Biosystems) at 97°C for 30 minutes prior to quenching endogenous peroxidase activity with 3% hydrogen peroxide. *Mtb* was identified using RNAscope 2.5 LS Probes B-MTB-23SrRNA-1-C1 (Advanced Cell Diagnostics #471658) and B-MTB-pre-rRNA-O1-C2 (Advanced Cell Diagnostics # 507548-C2) diluted 1:50 in the C1 probe (31, 35). ISH probes were visualized using TSA plus tetramethylrhodamine (Akoya Biosciences) at a dilution of 1:750, TSA plus fluorescein (Akoya Biosciences) at a dilution of 1:1000, and TSA plus cyanine 5 (Akoya Biosciences) at a dilution of 1:750 in 1X TSA Plus Automation Amplification Diluent (Akoya Biosciences). Nuclei were counterstained with DAPI

(Advanced Cell Diagnostics). Whole stained lung sections were scanned at 40X magnification using an Olympus VS120 microscope, Hamamatsu ORCA-R2 camera, and Olympus VS-ASW 2.9 software at the Experimental Pathology Facility at CSU. Exposure times were determined using the autoexposure function and adjusted to distinguish specific probe hybridization signal from erythrocyte background.

2.8 Multiplex fluorescent image analysis

Whole slide images were imported into Visiopharm image analysis software. Granulomas were identified using a decision forest algorithm trained on intensity and density of all fluorophores. Granulomas identified were confirmed or corrected based on annotations acquired from detection on H&E-stained slides. Each granuloma was then automatically assigned a unique ROI number within each lobe using the enumeration function in Visiopharm. Next, using a threshold-based algorithm, nuclei were detected and annotated based on DAPI signal intensity and given margins to allow for membrane analysis. For IHC, membranes were detected based on a threshold intensity of each fluorophore and assigned to their corresponding marker. For ISH, bacilli were detected based on a threshold intensity of the fluorophore assigned to the 23S rRNA probe, and further designated as replicating or non-replicating based on intensity of the corresponding fluorophore assigned to the pre-rRNA probe. In both IHC and ISH, red blood cell autofluorescence was accounted for based on low DAPI signal intensity combined with inherent combined signals of both FITC and tetramethylrhodamine. Thresholds for all markers were adjusted for any differences in staining or imaging quality and then reviewed for accuracy. Following review, counts for each cell type were quantified using an additional Visiopharm algorithm and exported as .csv files for downstream data analysis.

2.9 Statistical analysis

Statistical data analysis was performed in R (version 4.3.1). Data, code, and R packages from this study can be accessed through GitHub (https://github.com/PodellLab/Granuloma_RSRatio_ISH). Data exported from Visiopharm were pre-processed to prepare for downstream analysis in R. Preliminary exploratory statistical and graphical testing were performed to evaluate data distribution and differences between treatment groups. An unpaired t-test was used as a preliminary approach to calculate differences in granuloma burden, CFUs, and ISH RS ratios across treatment groups and infection endpoints.

Next, we fit a regression model to investigate the degree to which the immune cell populations in a granuloma are associated with the number of replicating bacteria in that granuloma, adjusting for the total number of bacteria in the granuloma. To do this, we fit a regression model with the number of replicating bacteria in a granuloma as the outcome variable and with three immune cell populations as potential explanatory variables, while controlling for

the timepoint and vaccination status and offsetting by the total number of bacteria. To make model coefficients more interpretable, we scaled immune cell counts by dividing by 500, based on the approximate interquartile range of each of these cell populations across the full study data. Therefore, the estimated coefficients represent an expected change per approximately one interquartile-range change in an immune cell population. Specifically, we fit the following quasi-Poisson regression model, adjusting for potential overdispersion of observed count data from each granuloma and including as an offset the log transformation of total bacterial counts measured by ISH:

$$\log(\lambda_i) = \beta_0 + \beta_1 X_{1,i} + \beta_2 X_{2,i} + \beta_3 X_{3,i} + \beta_4 X_{4,i} + \beta_5 X_{5,i} + \log(T_i)$$

Where, for each granuloma i :

- λ_i : Expected count of replicating *Mtb*
- $X_{1,i}$: Scaled count of B cells
- $X_{2,i}$: Scaled count of CD4 cells
- $X_{3,i}$: Scaled count of CD8 cells
- $X_{4,i}$: Indicator of vaccine status of the mouse with granuloma i , where unvaccinated is 0 and BCG-vaccinated is 1
- $X_{5,i}$: Indicator of infection endpoint of the mouse with granuloma i , where day 56 is 0 and day 114 is 1
- T_i : Total count of *Mtb* (replicating and non-replicating) in granuloma i
- $\beta_0 - \beta_5$: Model coefficients estimated from the data

3 Results

3.1 At the whole tissue level, BCG vaccination mediates reduction in culturable *Mtb* burden and total pulmonary pathology burden

Lung lobes were collected at necropsy at days 56 and 114 post-infection to assess *Mtb* burden at the level of the whole lung tissue. Colony forming units (CFU) of culturable bacteria in lung homogenate increased between day 56 and day 114 post-infection in both unvaccinated and BCG-vaccinated mice. However, BCG-vaccinated mice displayed reduced CFU burden at both days 56 and 114 post-infection compared to unvaccinated mice (Figure 1A). To establish whether the BCG vaccination offers protection from progressive pulmonary pathology at days 56 and 114 post-infection, the granuloma lesion burden was quantified histologically across the whole lung lobe using image analysis software (Figure 1B). Consistent with CFU at day 56, a significant decrease in granuloma lesion burden was observed in BCG-vaccinated mice compared to unvaccinated mice at day 56. Between day 56 and day 114 post-infection, the overall granuloma lesion burden increased in both groups. A decreased granuloma lesion burden was observed in BCG-vaccinated mice at day 114 post-infection although not statistically significant (Figure 1C).

3.2 Immune protection is demonstrated in whole lung granuloma lesion burden with histologically divergent features

Regardless of differences across pulmonary pathology burden, heterogeneity could be observed in morphological structure and cell composition among individual granulomas within an individual mouse, within vaccination status, and within infection endpoints (Figures 1D–I). H&E-stained lungs demonstrated granulomas with morphology of multiple and variable subtypes as observed by the reviewing pathologist (Podell BK). Granulomas were observed that consist of large centralized lymphoid aggregates resembling *de novo* tertiary lymphoid structures, some of which contain follicular centers composed of cells with macrophage-type morphology. Lymphoid structures are surrounded by either dense and eosinophilic epithelioid macrophages that replace pulmonary

architecture (Figures 1D, E), or alveolitis consisting of loose aggregates of heavily vacuolated macrophages contained within remnant alveolar spaces (Figures 1H, I). Other granulomas consisted of multiple smaller and less organized lymphoid aggregates surrounded by heavily vacuolated macrophages or have a paucity of lymphocyte cells and consist almost entirely of vacuolated macrophages. Among a proportion of the granulomas with poorly organized lymphoid structures, the heavily vacuolated macrophages were surrounded by alveolar interstitial fibrosis embedding small foci of necrosis with a high frequency of neutrophils (Figures 1F, G). While measures of granuloma lesion burden offer an indication of immune protection across the whole lung, this fails to encompass the heterogeneity of histological morphology observed across granulomas. This degree of histological heterogeneity suggests that distinct and diverse immune responses exist within and between mice, irrespective of

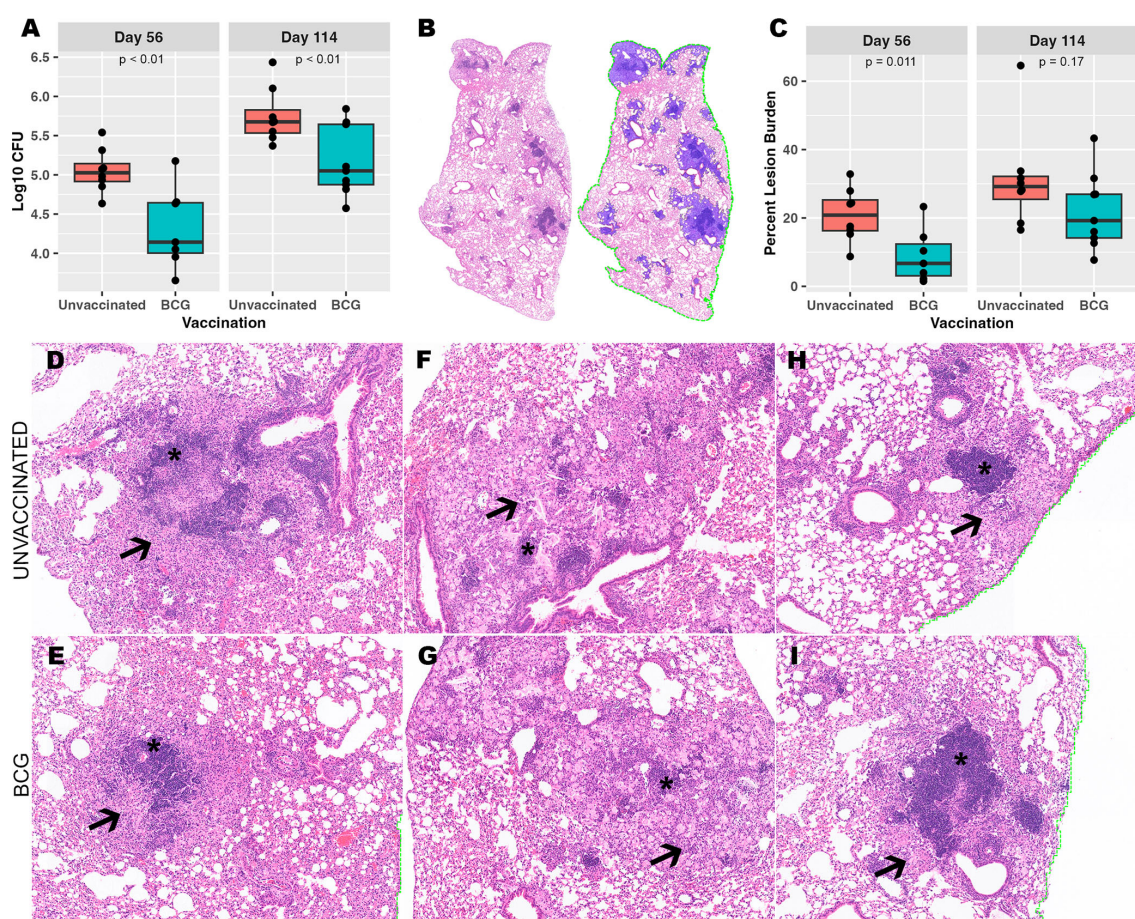


FIGURE 1

Despite BCG vaccine-mediated reduction in culturable bacterial burden, a heterogeneous granuloma response is shared across both vaccinated and unvaccinated mice. (A) Culturable *Mtb* colony forming units (CFU) in BCG-vaccinated and unvaccinated mice from left lung lobe tissue homogenates at day 56 and day 114 post-infection. (B) Right caudal lung lobes were H&E-stained after both timepoints of *Mtb* infection. A representative example is provided of a BCG-vaccinated mouse to identify and quantify granuloma lesion burden using Visiopharm image analysis software where granulomas (left) are detected across the entire lung lobe section as shown with blue overlay (right). (C) Percent granuloma lesion burden separated by infection endpoint and vaccination status; each point represents a lung section from an individual mouse. (D–I) Granulomas with diverse morphology shared between unvaccinated and BCG-vaccinated mice. (D, E) Loose centralized aggregates of lymphocytes (asterisk) surrounded by epithelioid macrophages (arrow). (F, G) Scattered small lymphocyte aggregates (asterisk) surrounded by heavily vacuolated macrophages, neutrophils and foci of necrosis embedded within areas of alveolar interstitial fibrosis (arrow). (H, I) Centralized dense lymphoid aggregates (asterisk) surrounded by vacuolated macrophages (arrow) and discrete granuloma boundaries. Images provided at 50X magnification.

vaccination, and that granuloma targeted analysis could offer greater insight into correlates of protection that cannot be observed through bulk tissue analyses.

3.3 Quantification of replicating *Mtb* by ISH RS ratio reveals heterogeneity in immune control of *Mtb* replication across granulomas

Divergent features of granuloma histomorphology suggest a more granular measure of bacterial replication may distinguish differences between granulomas. To better understand each granuloma's ability to control bacterial replication, multiplexed fluorescent *in situ* hybridization (ISH), using targets analogous to the RS ratio dPCR (31, 35), was employed to visualize individual replicating and nonreplicating *Mtb* organisms, referred to as RS ratio ISH. In this approach, a replicating bacillus was defined by colocalized detection of both ETS1/ITS1 pre-rRNA sequence and mature 23S rRNA sequence, while a non-replicating *Mtb* bacillus was defined by detection of 23S rRNA only. 191 granulomas identified on H&E-stained slides were evaluated (Table 1). The number of granulomas per mouse tended to be higher in unvaccinated mice at day 56 post-infection compared to BCG-vaccinated mice, but increased in number among BCG-vaccinated mice between day 56 and day 114 post-infection. 23S rRNA and ETS1/ITS1 pre-rRNA detection was quantified using Visiopharm image analysis software and the proportion of replicating bacteria relative to total bacteria calculated (Figures 2A–D). At both days 56 and day 114 post-infection, granulomas from unvaccinated mice displayed higher proportions of replicating *Mtb* compared to BCG-vaccinated animals (Figure 2E). Collectively, the proportions of replicating *Mtb* decreased across granulomas between day 56 and day 114, irrespective of vaccination status. Regardless of timepoint or vaccination status, a wide range of total bacterial burden and

replication status was observed between and within groups and within individual animals.

Considering the heterogeneity of replicating proportions of *Mtb* observed across the granuloma, a direct comparison was made to the whole lung CFU per mouse that, as a stand-alone metric, supports vaccine-mediated protection. In comparing these metrics, it is evident that regardless of CFU value, granulomas per mouse vary in number. Within and between mice, these granulomas display an expansive range of total *Mtb* burden and proportion of replicating *Mtb* by ISH. There was no evident directional association between replicating *Mtb* by RS ratio ISH and culturable *Mtb* burden by CFU (Figure 2F). Rather, CFUs appear to more linked to the total number of granulomas in the mouse. These data suggest that total CFU burden reflects a collective contribution of diverse granuloma responses with differing capacities to control *Mtb* replication. Overall, the results from granuloma-targeted RS ratio ISH highlights that a wide range of capacity for immune control of *Mtb* replication exists across granulomas, which cannot be effectively captured by CFU. Thus, RS ratio ISH may distinguish granulomas with immune cell composition that provide greater control of *Mtb* replication.

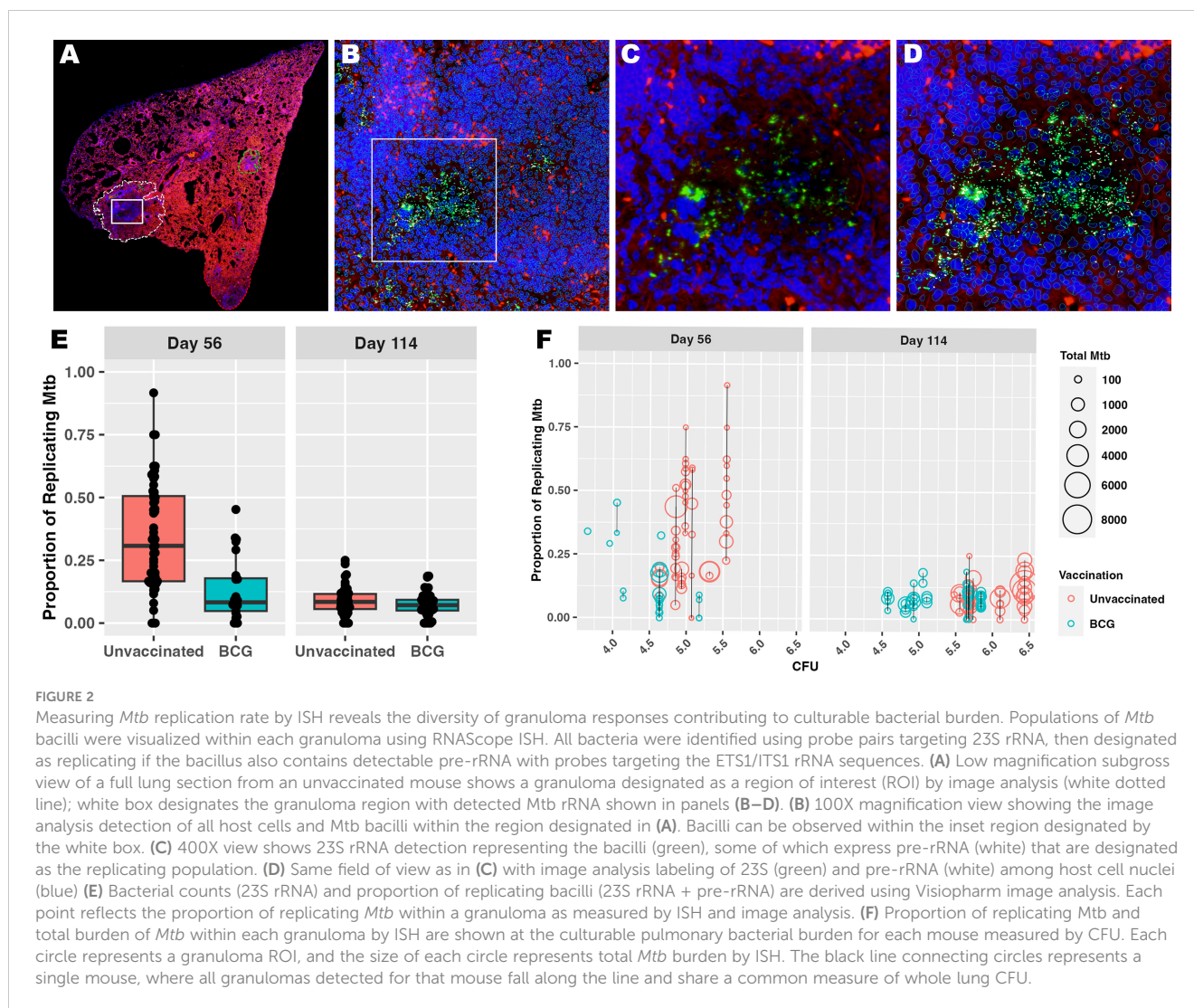
3.4 Granulomas exhibit divergent composition of adaptive immune cell phenotypes by IHC

We investigated underlying spontaneous and BCG-induced adaptive immunity by multiplexed IHC in conjunction with the granuloma heterogeneity observed both histologically and in *Mtb* replication rate by RS ratio ISH. Essential adaptive immune cell phenotypes were considered because previous work shows a reduction in total lung RS ratio at the onset of adaptive immunity (31). Accordingly, CD4 cells, CD8 cells, B cells, and other host cells were targeted within granulomas in which the RS ratio ISH was

TABLE 1 Granuloma-level measures of host cells and *Mtb*.

	Day 56			Day 114		
	Unvaccinated (n = 59)	Vaccinated (n = 24)	Overall (n = 83)	Unvaccinated (n = 55)	Vaccinated (n = 53)	Overall (n = 108)
Host	Median Count			Median Count		
CD4 T cell	162	90	157	261	449	320
CD8 T cell	169	170	169	219	355	259
B cell	137	95	116	154	387	234
Other	2036	1952	2036	2407	2601	2436
Total	2441	2325	2424	3205	3538	3337
Mtb	Median Count			Median Count		
Replicating	19 (22.6%)	2.5 (5.3%)	13 (18.3%)	28 (7.1%)	13 (6.8%)	15.5 (6.6%)
Nonreplicating	51	37	46	368	183	213.5
Total	84	47	71	393	190	236

Counts of granulomas in each group are indicated by n.



quantified (Table 1). Within each granuloma designated as an independent ROI, each cell subset was identified and quantified using Visiopharm image analysis software (Figures 3A–D). Granulomas displayed heterogeneous cellular composition and organization across all groups and endpoints evaluated, where total cell counts of any measured phenotype are unable to distinguish vaccine status or day of infection (Figure 3E). All measured immune cells increase in median number per granuloma between day 56 and day 114, and this increase remained similar across B cells, CD4, and CD8 cells, but these changes between infection endpoints are small in comparison to the large variability observed within each group. The most prevalent cell type at either day 56 or day 114 are those that do not belong to any of the three evaluated phenotypes and are designated by the term, “other cells”. Overall, a wide spread of cell counts was observed independent of timepoint or vaccination status, exemplifying differences across granulomas that may provide context for ability to control bacterial replication.

3.5 Relative rate of *Mtb* replication is inversely associated with CD4 and CD8 cell composition at the granuloma level

Having established granuloma heterogeneity in the C57BL/6 mouse model using simultaneous measures of host and bacterial response, we then performed regression analysis to identify any association with immune environments capable of controlling *Mtb* replication. To do so, a generalized linear regression model was utilized to determine associations between immune cell composition and counts of replicating *Mtb*, while accounting for total *Mtb* burden through a model offset. Based on differences between interquartile ranges (IQR) among immune cells, counts of immune cells were scaled down by a factor of 500 to approximate the IQR, which facilitates interpretation of respective comparisons. Controlling for all variables, irrespective of vaccine status or timepoint, an inverse relationship between CD4 and CD8 cells was observed with changes in the relative rate of bacterial replication. A 17.7% decrease in estimated relative rate

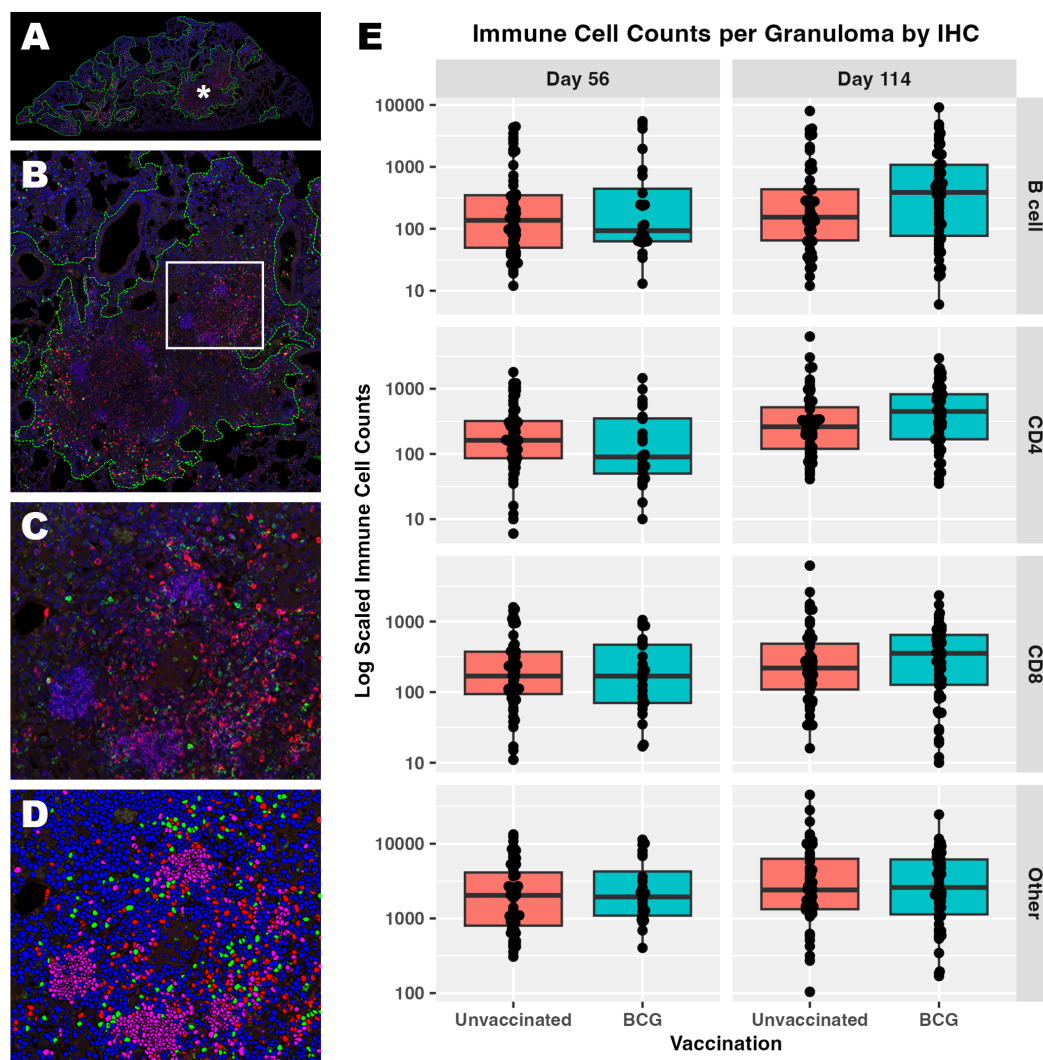


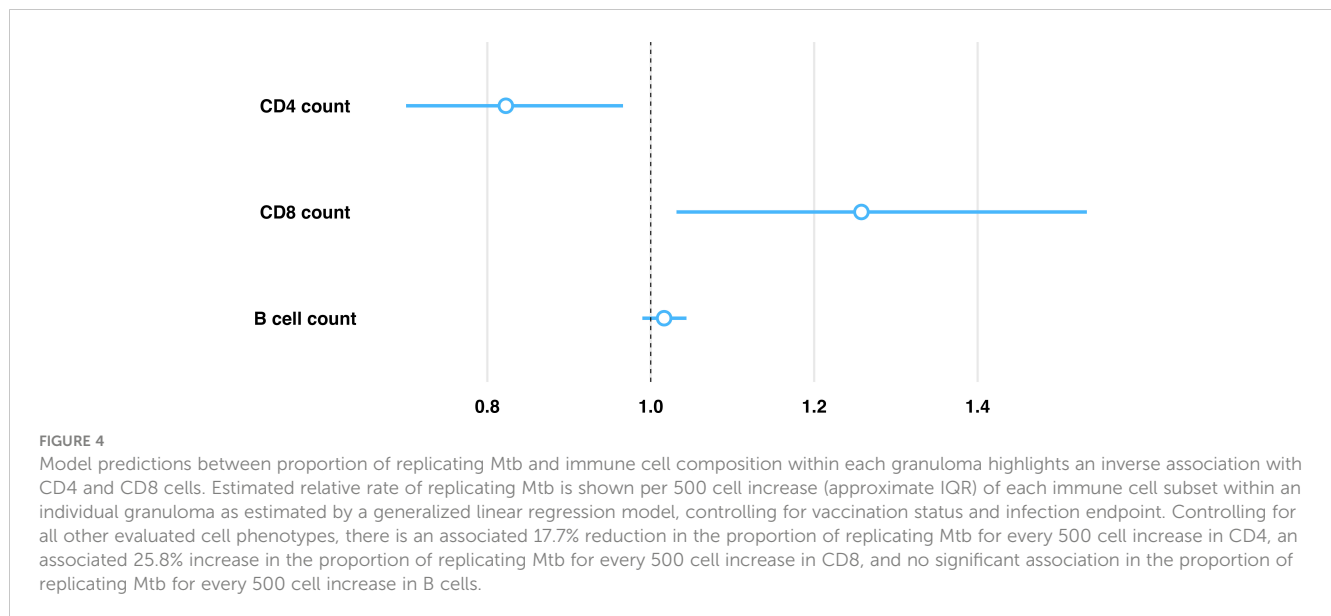
FIGURE 3

Immune cell composition of granulomas identifies a wide degree of host heterogeneity that alone cannot distinguish trends in immune protection. Populations of CD4, CD8, and B cells were visualized within each granuloma using multiplexed fluorescent IHC with a DAPI nuclear counterstain. (A) Low magnification subgross view of a full lung section from an unvaccinated mouse shows granulomas designated as regions of interest (ROI) by image analysis (green dotted lines). (B) Higher magnification view of the granuloma ROI designated by the asterisk in (A). (C) Immune subsets are demonstrated at 200x magnification within the inset region designated by the white box in B; B cells (pink), CD4 cells (green), CD8 cells (red). (D) The same 200X view as in (C) is shown with each immune subset or 'other cell' designated using image analysis; B cells (pink), CD4 cells (green), CD8 cells (red), other cells (blue, DAPI only). Nuclei detected that do not belong to either CD4, CD8, or B cell are classified as other. (E) Cell counts detected at day 56 and day 114 post-infection within each granuloma ROI. Each point represents a granuloma.

of *Mtb* replication was associated with each 500-cell increase in CD4, and a 25.8% increase in relative rate of *Mtb* replication was associated with each 500-cell increase in CD8, while B cell count showed no significant association with *Mtb* replication (Figure 4). Controlling for differences in these host cell populations, BCG vaccination was associated with a 35.4% decrease in estimated relative rate of replication compared to unvaccinated, while progression to day 114 post-infection was associated with a 54.7% decrease over time compared to day 56 post-infection. Here we identify a significant association between granuloma immune cell composition and control of *Mtb* replication. Data obtained from all evaluated granulomas, including immune cell counts and replication rates are available at https://github.com/PodellLab/Granuloma_RSratio_ISH.

3.6 Histologic morphology of granulomas is consistent with immune cell counts and rate of *Mtb* replication

Based on predictions using this model, we back-translated associations between cell composition and RS ratio ISH replication rates to evaluate granuloma morphology associated with immune control of bacterial replication. Selection of two granulomas from the lung lobe of a single BCG-vaccinated mouse at day 56 post-infection highlights the observation that different degrees of bacterial replication existing between granulomas is associated with immune cell composition unique to each granuloma (Figure 5). Between these two granulomas within this



single mouse, CD8 cells differ by 547 cells and *Mtb* replication is increased by 28.9% (Table 2). Consistent with the multiple morphologies described in Figure 1, these granulomas contain either higher proportions of vacuolated macrophages or epithelioid macrophages and B cell-rich *de novo* follicular structures. In these granulomas, the higher *Mtb* replication rate is localized to macrophages with vacuolated morphology, which is overrepresented in the granuloma with the higher CD8 count. These findings indicate that cell populations with a designated morphology may align with poor control of *Mtb* replication. Furthermore, granuloma morphology may indicate an immune environment with capacity to successfully limit, or fail to control, *Mtb* replication.

4 Discussion

In this study, we applied the RS ratio through *in situ* hybridization (RS ratio ISH) to identify the frequency of new rRNA production, which serves as a proxy measure of *Mtb* replication (31, 35). Here, we identified the replicative response of *Mtb* to immune pressure over two chronic endpoints of infection and in response to BCG vaccination. A wide range of *Mtb* replication states was demonstrated across granulomas both within individual animals, as well as between animals evaluated at the same infection endpoint, independent of respective vaccination status. These results highlight the extensive degree of heterogeneity among *Mtb* replicative states across granulomas. We found that culturable bacterial burden from whole lung homogenate, as determined by CFU, does not necessarily reflect the spectrum of *Mtb* replication states across granulomas. Although vaccination does reduce CFU, the difference in *Mtb* replication rate remains similar in some granulomas of BCG-vaccinated mice, compared to unvaccinated mice. Additionally, these data indicate that rate of replication within a granuloma and total bacterial burden do not necessarily correlate. In many instances, granulomas with the

highest rate of *Mtb* replication do not have the highest burden of bacteria, as identified by detection of 23S rRNA alone. These data suggest that a differential host response may exist between granulomas with high or low replication rates, or those with high or low *Mtb* burden. We hypothesized discrimination of these immune environments and their overarching contribution to the replicative state of the *Mtb* bacilli may identify correlates of protective responses.

We identified a wide diversity of granuloma compositions, containing varying frequencies of CD4, CD8 and B cell populations, which is consistent with the highly heterogeneous replication rates of *Mtb* across granulomas. These findings are inconsistent with the constrained host immune response characteristic of the C57BL/6 mouse strain. These mice have a well-documented Th1 skewed cell-mediated immune response with granulomas described as lacking advanced pathology features (3). Despite an apparent uniformity in the immune response to *Mtb* infection, our findings indicate that granuloma heterogeneity exists in C57BL/6 mice, highlighting the importance of granuloma-targeted analysis. This approach provides an adjunctive method to distinguish granuloma-specific differences in immune response within and between animals enabling determination of the local granuloma response as opposed to whole tissue measures, such as flow cytometry.

To determine if the variability in *Mtb* replicative state is associated with differences in host response, we established a generalized linear regression model to evaluate the association between *Mtb* replication rate and CD4, CD8 and B cell populations across nearly 200 granulomas. Based on culturable CFU, these broad phenotypic categories have an established role in TB disease as a primary outcome measure. However, due to previous limitations in concurrent host and pathogen *in situ* analyses, determining associations between each immune cell subset and the *Mtb* bacterial replication state was not achievable. Using multiplexed IHC and RS ratio ISH to assess both host phenotype frequency and bacterial replication rate, we

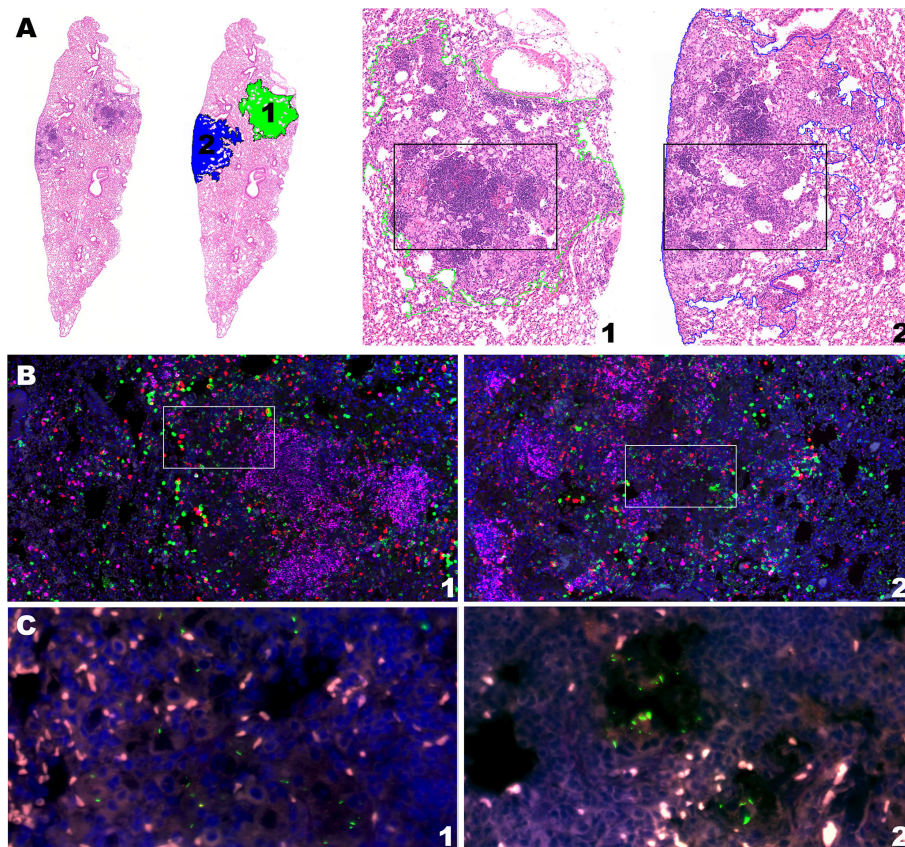


FIGURE 5

Intramouse heterogeneity in granuloma morphology, immune cell composition, and *Mtb* replication rate aligns with model predictions. Two neighboring granulomas within the same lung section of the same BCG-vaccinated mouse are shown by H&E stain, multiplexed IHC, and RS ratio ISH. (A) H&E stain at subgross showing the ROI of granuloma 1 and 2 from the BCG-vaccinated mouse (10X magnification) at day 56 post-infection and H&E morphology of each granuloma outlined by green and blue dotted lines for granulomas 1 and 2, respectively (50X magnification). (B) Multiplexed IHC demonstrating populations of CD4 cells (green), CD8 cells (red) and B cells (pink) in granulomas 1 and 2 (100X magnification). White boxes indicate inset regions for visualization of *Mtb* organisms. (C) *Mtb* bacilli detected with pre-rRNA and 23S rRNA probes by RNAScope ISH in granulomas 1 and 2.

determined the association between immune cell composition and the respective response of the bacterial population within each granuloma. Through this, a unique association between CD4 and CD8 cell frequencies and *Mtb* replication rates has been established in any individual granuloma, while a statistically significant association between B cells and *Mtb* replication rate was not observed in the evaluated granulomas.

Our model indicated that every unit increase in CD4 cells was associated with a significant decrease in *Mtb* replication rate, while every unit increase in CD8 cells was associated with a significant increase in *Mtb* replication rate. Although CD4 and CD8 cells have established roles in the constraint of *Mtb* growth in tissue, the opposing directionality of each cell type association may suggest different roles for CD4 and CD8 cells in the granuloma response. However, this relationship does not yet indicate any directional causality despite definitive associations. In this context, the RS ratio measure of replication rate may inform further investigation of granuloma response where further interventions that manipulate specific host cell phenotypes are needed to determine the mechanism by which a designated cell type contributes to immune control of *Mtb* replication.

In concordance with the granuloma-level degree of heterogeneity in both host and bacterial populations, differences in granuloma morphology based on traditional H&E-stained slides were observed. In multiple conventional inbred mouse strains, including the C57BL/6 mouse, tertiary lymphoid follicular structures are a frequent and dominant feature of the response to *Mtb* infection (36, 37). Granulomas can be distinguished as having either dense and well-structured follicles, or loosely organized lymphoid infiltration. Further, the innate populations of macrophages may be either heavily vacuolated or more epithelioid in appearance. Vacuolated macrophage populations may contain varying levels of accompanying neutrophils and cellular fragmentation consistent with multiple mechanisms of macrophage cell death. We found that intragranuloma follicular structures are heavily dominated by B cells and have limited T cell involvement. Although some granulomas have high proportions of follicle-associated B cells, our model indicated no statistical association with *Mtb* replication rate. In contrast, we histologically observed that granulomas with high CD4 T cell frequencies and lower *Mtb* replication rates contained more epithelioid macrophage populations. Granulomas with high CD8

TABLE 2 Individual granuloma measures informing histopathology morphological features.

	BCG 24–1	BCG 24–2
Proportion replicating <i>Mtb</i>	0.142	0.183
Replicating <i>Mtb</i>	27	43
Nonreplicating <i>Mtb</i>	163	192
Total <i>Mtb</i>	190	235
CD8 count (%)	774	1321
CD4 count (%)	1082	1027
B220 count (%)	3286	3485
Other cell count (%)	9097	11638
CFU (Log ₁₀ per g tissue)	5.05	5.05

Examples of granulomas highlighting histopathological morphology based on GLM associations are shown in Figure 5. Characteristics of each of granuloma are identified by individual mouse-granuloma (i.e., 24–1). Data for all granulomas evaluated in this study are available on the GitHub repository.

T cells and high *Mtb* replication rates contained prominent vacuolated macrophage populations. Further *in situ* investigation of unique H&E-defined granuloma morphology may reflect critical microenvironmental differences in host response, including host immune cell composition, and subsequently constraint of *Mtb* replication (38).

The key associations in immune cell composition and bacterial replication rate revealed by our model leads us to ask the question ‘does restriction of *Mtb* replication represent an ideal pathogen-targeted measure of immune protection?’. *Mtb* has an inherent capacity to enter a dormancy-like phenotype, and previous studies using progressive hypoxia models of *in vitro* grown *Mtb* suggests that dormancy onset accompanies a reduction in replication (31, 39). Such dormant phenotypes may contribute less to progressive TB disease (40, 41). Increased dormancy induced by immune pressure on the *Mtb* bacilli may be associated with an altered treatment response (42) or may reflect a temporary replicative constraint on the *Mtb* population (43), which may recover following changes in the immune environment. Alternatively, a reduced replication rate could reflect improved control of bacterial growth and an increase in bacteriostatic effect from the ongoing immune response (44–46). Distinguishing dormancy from other mechanisms of immune constraint on *Mtb* replication requires further investigation of the bacterial response *in situ*. This presents its own challenges but may be determined by emerging techniques, such as SearchTB, using *Mtb* enriched extracts from tissue (47).

There are limitations to this study and this method. The evaluation of only three adaptive immune cell phenotypes, B cells, CD4 and CD8 T cells, underrepresents the complexity of the TB granuloma (48). This is evident based on recent single cell RNA seq studies that have demonstrated 18 distinct lymphoid cell subpopulations involved in the pulmonary granulomatous response of murine TB models (20). We recognize the power of adjunctive

immunological methods (i.e. flow cytometry, scRNAseq) in assessing host protection as well as the greater capacity of these methods to identify specific details of the host response. However, this study serves as proof-of-concept that granulomas with differing cell compositions also have distinct differences in capacity to influence *Mtb* replication. Additionally, the results presented here represent only one context of a modeled *Mtb* infection, that of unvaccinated and BCG-vaccinated C57BL/6 mice infected by low-dose aerosol exposure to the Erdman strain. The application of this approach to other model strains, species, vaccine compositions, and strains of *Mtb* will further elucidate the capacity for granuloma targeted analysis to identify correlates of immune protection. The RS ratio used here provides adjunctive value to whole tissue measures, with the distinct advantage of evaluating the concurrent host and *Mtb* bacterial response *in situ* within any given granuloma. The RS ratio ISH method is not intended to serve as an alternative or replacement for CFU determination as a measurement of TB disease outcome. Rather, this approach offers orthogonal information to culturable bacterial burden by providing critical information on the *Mtb* replicative state in the native granuloma microenvironment that cannot be measured by CFU alone (31). The ongoing development and implementation of complementary granuloma and whole lung methodologies holds promise for advancing our understanding of TB and facilitating development and assessment of effective vaccines and therapeutics.

Data availability statement

The datasets presented in this study can be found in online repositories. The names of the repository/repositories and accession number(s) can be found below: https://github.com/PodellLab/Granuloma_RSratio_ISH.

Ethics statement

The animal study was approved by Colorado State University Institutional Animal Care and Use Committee. The study was conducted in accordance with the local legislation and institutional requirements.

Author contributions

SC: Data curation, Formal analysis, Investigation, Methodology, Validation, Visualization, Writing – original draft, Writing – review & editing. DA: Data curation, Formal analysis, Investigation, Methodology, Writing – review & editing. FL: Conceptualization, Investigation, Resources, Supervision, Visualization, Writing – review & editing. MH-T: Conceptualization, Funding acquisition, Project administration, Resources, Supervision, Writing – review & editing. GBA: Conceptualization, Data curation, Formal analysis, Investigation, Methodology, Project administration, Resources,

Software, Supervision, Writing – original draft, Writing – review & editing. BP: Conceptualization, Formal analysis, Funding acquisition, Investigation, Methodology, Project administration, Resources, Supervision, Validation, Visualization, Writing – original draft, Writing – review & editing.

Funding

The author(s) declare financial support was received for the research, authorship, and/or publication of this article. This project has been funded in whole or in part with federal funds from the National Institute of Allergy and Infectious Diseases, National Institutes of Health, Department of Health and Human Services, under Phoenix Immune Mechanisms of Protection Against Tuberculosis Centers (IMPAC-TB) 75N93021C00029 and by the National Institute Of Allergy And Infectious Diseases of the National Institutes of Health under Award Number T32AI162691. The content is solely the responsibility of the authors and does not necessarily represent the official views of the National Institutes of Health.

Acknowledgments

The authors would like to acknowledge the service provided by the histology laboratory at the Veterinary Diagnostic Laboratory for their contributions to histology processing and the Experimental Pathology Facility at Colorado State University, RRID: SCR_23562, for access to automated immunostaining instrumentation and Visiopharm image analysis software.

References

- Paige C, Bishai WR. Penitentiary or penthouse condo: the tuberculous granuloma from the microbe's point of view. *Cell Microbiol.* (2010) 12:301–9. doi: 10.1111/cmi.2010.12.issue-3
- Cadena AM, Fortune SM, Flynn JL. Heterogeneity in tuberculosis. *Nat Rev Immunol.* (2017) 17:691–702. doi: 10.1038/nri.2017.69
- Lenaerts A, Barry CE 3rd, Dartois V. Heterogeneity in tuberculosis pathology, microenvironments and therapeutic responses. *Immunol Rev.* (2015) 264:288–307. doi: 10.1111/imr.12252
- Chen RY, Dodd LE, Lee M, Paripati P, Hammoud DA, Mountz JM, et al. PET/CT imaging correlates with treatment outcome in patients with multidrug-resistant tuberculosis. *Sci Transl Med.* (2014) 6:265ra166. doi: 10.1126/scitranslmed.3009501
- Coleman MT, Maiello P, Tomko J, Frye LJ, Fillmore D, Janssen C, et al. Early Changes by (18)Fluorodeoxyglucose positron emission tomography coregistered with computed tomography predict outcome after Mycobacterium tuberculosis infection in cynomolgus macaques. *Infect Immun.* (2014) 82:2400–4. doi: 10.1128/IAI.01599-13
- Esmail H, Lai RP, Lesosky M, Wilkinson KA, Graham CM, Coussens AK, et al. Characterization of progressive HIV-associated tuberculosis using 2-deoxy-2-[(18)F] fluoro-D-glucose positron emission and computed tomography. *Nat Med.* (2016) 22:1090–3. doi: 10.1038/nm.4161
- Wells G, Glasgow JN, Nargan K, Lumamba K, Madansei R, Maharaj K, et al. A high-resolution 3D atlas of the spectrum of tuberculous and COVID-19 lung lesions. *EMBO Mol Med.* (2022) 14:e16283. doi: 10.15252/emmm.202216283
- Sawyer AJ, Patrick E, Edwards J, Wilmott JS, Fielder T, Yang Q, et al. Spatial mapping reveals granuloma diversity and histopathological superstructure in human tuberculosis. *J Exp Med.* (2023) 220(6):e20221392. doi: 10.1084/jem.20221392
- Capuano SV 3rd, Croix DA, Pawar S, Zinovik A, Myers A, Lin PL, et al. Experimental Mycobacterium tuberculosis infection of cynomolgus macaques closely resembles the various manifestations of human M. tuberculosis infection. *Infect Immun.* (2003) 71:5831–44. doi: 10.1128/IAI.71.10.5831-5844.2003
- Lin PL, Maiello P, Gideon HP, Coleman MT, Cadena AM, Rodgers MA, et al. PET CT identifies reactivation risk in cynomolgus macaques with latent M. tuberculosis. *PLoS Pathog.* (2016) 12:e1005739. doi: 10.1371/journal.ppat.1005739
- Irwin SM, Driver E, Lyon E, Schrupp C, Ryan G, Gonzalez-Juarrero M, et al. Presence of multiple lesion types with vastly different microenvironments in C3HeB/FeJ mice following aerosol infection with Mycobacterium tuberculosis. *Dis Model Mech.* (2015) 8:591–602. doi: 10.1242/dmm.019570
- Plumlee CR, Barrett HW, Shao DE, Lien KA, Cross LM, Cohen SB, et al. Assessing vaccine-mediated protection in an ultra-low dose Mycobacterium tuberculosis murine model. *PLoS Pathog.* (2023) 19:e1011825. doi: 10.1371/journal.ppat.1011825
- Plumlee CR, Duffy FJ, Gern BH, Delahaye JL, Cohen SB, Stoltzfus CR, et al. Ultra-low dose aerosol infection of mice with mycobacterium tuberculosis more closely models human tuberculosis. *Cell Host Microbe.* (2021) 29:68–82 e5. doi: 10.1016/j.chom.2020.10.003
- Basaraba RJ, Smith EE, Shanley CA, Orme IM. Pulmonary lymphatics are primary sites of Mycobacterium tuberculosis infection in Guinea pigs infected by aerosol. *Infect Immun.* (2006) 74:5397–401. doi: 10.1128/IAI.00332-06
- Henao-Tamayo M, Shanley CA, Verma D, Zilavy A, Stapleton MC, Furney SK, et al. The Efficacy of the BCG Vaccine against Newly Emerging Clinical Strains of Mycobacterium tuberculosis. *PLoS One.* (2015) 10:e0136500. doi: 10.1371/journal.pone.0136500

Conflict of interest

The authors declare that the research was conducted in the absence of any commercial or financial relationships that could be construed as a potential conflict of interest.

The author(s) declared that they were an editorial board member of Frontiers, at the time of submission. This had no impact on the peer review process and the final decision.

Publisher's note

All claims expressed in this article are solely those of the authors and do not necessarily represent those of their affiliated organizations, or those of the publisher, the editors and the reviewers. Any product that may be evaluated in this article, or claim that may be made by its manufacturer, is not guaranteed or endorsed by the publisher.

Author disclaimer

The content is solely the responsibility of the authors and does not necessarily represent the official views of the National Institutes of Health.

Supplementary material

The Supplementary Material for this article can be found online at: <https://www.frontiersin.org/articles/10.3389/fimmu.2024.1427472/full#supplementary-material>

16. Palanisamy GS, DuTeau N, Eisenach KD, Cave DM, Theus SA, Kreiswirth BN, et al. Clinical strains of *Mycobacterium tuberculosis* display a wide range of virulence in Guinea pigs. *TubercuL (Edinb)*. (2009) 89:203–9. doi: 10.1016/j.tube.2009.01.005
17. Lin PL, Ford CB, Coleman MT, Myers AJ, Gawande R, Ioegeer T, et al. Sterilization of granulomas is common in active and latent tuberculosis despite within-host variability in bacterial killing. *Nat Med*. (2014) 20:75–9. doi: 10.1038/nm.3412
18. Scanga CA, Mohan VP, Yu K, Joseph H, Tanaka K, Chan J, et al. Depletion of CD4(+) T cells causes reactivation of murine persistent tuberculosis despite continued expression of interferon gamma and nitric oxide synthase 2. *J Exp Med*. (2000) 192:347–58. doi: 10.1084/jem.192.3.347
19. Yao S, Huang D, Chen CY, Halliday L, Wang RC, Chen ZW. CD4+ T cells contain early extrapulmonary tuberculosis (TB) dissemination and rapid TB progression and sustain multifactor functions of CD8+ T and CD3- lymphocytes: mechanisms of CD4+ T cell immunity. *J Immunol*. (2014) 192:2120–32. doi: 10.4049/jimmunol.1301373
20. Akter S, Chauhan KS, Dunlap MD, Chorenno-Parra JA, Lu L, Esaulova E, et al. *Mycobacterium tuberculosis* infection drives a type I IFN signature in lung lymphocytes. *Cell Rep*. (2022) 39:110983. doi: 10.1016/j.celrep.2022.110983
21. Esaulova E, Das S, Singh DK, Chorenno-Parra JA, Swain A, Arthur L, et al. The immune landscape in tuberculosis reveals populations linked to disease and latency. *Cell Host Microbe*. (2020) 29(2):165–78.e8. doi: 10.1016/j.chom.2020.11.013
22. Chen Y, Bharrhan S, Xu J, Sharma T, Wang Y, Salgame P, et al. B cells promote granulomatous inflammation during chronic *Mycobacterium tuberculosis* infection in mice. *PLoS Pathog*. (2023) 19:e1011187. doi: 10.1371/journal.ppat.1011187
23. Lu LL, Das J, Grace PS, Fortune SM, Restrepo BI, Alter G. Antibody fc glycosylation discriminates between latent and active tuberculosis. *J Infect Dis*. (2020) 222:2093–102. doi: 10.1093/infdis/jiz643
24. Nizza N, Cizmeci D, Davies L, Irvine EB, Jung W, Fenderson BA, et al. Defining discriminatory antibody fingerprints in active and latent tuberculosis. *Front Immunol*. (2022) 13:856906. doi: 10.3389/fimmu.2022.856906
25. Booty MG, Nunes-Alves C, Carpenter SM, Jayaraman P, Behar SM. Multiple inflammatory cytokines converge to regulate CD8+ T cell expansion and function during tuberculosis. *J Immunol*. (2016) 196:1822–31. doi: 10.4049/jimmunol.1502206
26. Gideon HP, Hughes TK, Tzouanas CN, Wadsworth MH 2nd, Tu AA, Gierahn TM, et al. Multimodal profiling of lung granulomas in macaques reveals cellular correlates of tuberculosis control. *Immunity*. (2022) 55:827–46 e10. doi: 10.1016/j.immuni.2022.04.004
27. Yang JD, Mott D, Sutiwisesak R, Lu YJ, Raso F, Stowell B, et al. *Mycobacterium tuberculosis*-specific CD4+ and CD8+ T cells differ in their capacity to recognize infected macrophages. *PLoS Pathog*. (2018) 14:e1007060. doi: 10.1371/journal.ppat.1007060
28. Hoff DR, Ryan GJ, Driver ER, Ssemakulu CC, De Groot MA, Basaraba RJ, et al. Location of intra- and extracellular *M. tuberculosis* populations in lungs of mice and Guinea pigs during disease progression and after drug treatment. *PLoS One*. (2011) 6:e17550. doi: 10.1371/journal.pone.0017550
29. Ryan GJ, Shapiro HM, Lenaerts AJ. Improving acid-fast fluorescent staining for the detection of mycobacteria using a new nucleic acid staining approach. *TubercuL (Edinb)*. (2014) 94:511–8. doi: 10.1016/j.tube.2014.07.004
30. Vilcheze C, Kremer L. Acid-fast positive and acid-fast negative mycobacterium tuberculosis: the koch paradox. *Microbiol Spectr*. (2017) 5(2). doi: 10.1128/microbiolspec.TB2-0003-2015
31. Walter ND, Born SEM, Robertson GT, Reichlen M, Dide-Agossou C, Eknitphong VA, et al. *Mycobacterium tuberculosis* precursor rRNA as a measure of treatment-shortening activity of drugs and regimens. *Nat Commun*. (2021) 12:2899. doi: 10.1038/s41467-021-22833-6
32. Henao-Tamayo MI, Obregon-Henao A, Arnett K, Shanley CA, Podell B, Orme IM, et al. Effect of bacillus Calmette-Guerin vaccination on CD4+Foxp3+ T cells during acquired immune response to *Mycobacterium tuberculosis* infection. *J Leukoc Biol*. (2016) 99:605–17. doi: 10.1189/jlb.4A0614-308RR
33. Tiwari S, Dutt TS, Chen B, Chen M, Kim J, Dai AZ, et al. BCG-Prime and boost with *Esx-5* secretion system deletion mutant leads to better protection against clinical strains of *Mycobacterium tuberculosis*. *Vaccine*. (2020) 38:7156–65. doi: 10.1016/j.vaccine.2020.08.004
34. Larsen SE, Reese VA, Pecor T, Berube BJ, Cooper SK, Brewer G, et al. Subunit vaccine protects against a clinical isolate of *Mycobacterium avium* in wild type and immunocompromised mouse models. *Sci Rep*. (2021) 11:9040. doi: 10.1038/s41598-021-88291-8
35. Robertson GT, Ramey ME, Massoudi LM, Carter CL, Zimmerman M, Kaya F, et al. Comparative analysis of pharmacodynamics in the C3HeB/feJ mouse tuberculosis model for dprE1 inhibitors TBA-7371, PBTZ169, and OPC-167832. *Antimicrob Agents Chemother*. (2021) 65:e0058321. doi: 10.1128/AAC.00583-21
36. Dutt TS, Karger BR, Fox A, Youssef N, Dadhwal R, Ali MZ, et al. Mucosal exposure to non-tuberculous mycobacteria elicits B cell-mediated immunity against pulmonary tuberculosis. *Cell Rep*. (2022) 41:111783. doi: 10.1016/j.celrep.2022.111783
37. Rijnink WF, Ottenhoff THM, Joosten SA. B-cells and antibodies as contributors to effector immune responses in tuberculosis. *Front Immunol*. (2021) 12:640168. doi: 10.3389/fimmu.2021.640168
38. Walter ND, Ernest JP, Dide-Agossou C, Bauman AA, Ramey ME, Rossmassler K, et al. Lung microenvironments harbor *Mycobacterium tuberculosis* phenotypes with distinct treatment responses. *Antimicrob Agents Chemother*. (2023) 67:e0028423. doi: 10.1128/aac.00284-23
39. Voskuil MI, Schnappinger D, Visconti KC, Harrell MI, Dolganov GM, Sherman DR, et al. Inhibition of respiration by nitric oxide induces a *Mycobacterium tuberculosis* dormancy program. *J Exp Med*. (2003) 198:705–13. doi: 10.1084/jem.20030205
40. Scanga CA, Mohan VP, Joseph H, Yu K, Chan J, Flynn JL. Reactivation of latent tuberculosis: variations on the Cornell murine model. *Infect Immun*. (1999) 67:4531–8. doi: 10.1128/IAI.67.9.4531-4538.1999
41. van Pinxteren LA, Cassidy JP, Smedegaard BH, Agger EM, Andersen P. Control of latent *Mycobacterium tuberculosis* infection is dependent on CD8 T cells. *Eur J Immunol*. (2000) 30:3689–98. doi: 10.1002/(ISSN)1521-4141
42. Sarathy JP, Via LE, Weiner D, Blanc L, Boshoff H, Eugenin EA, et al. Extreme drug tolerance of mycobacterium tuberculosis in caseum. *Antimicrob Agents Chemother*. (2018) 62(2):e02266-17. doi: 10.1128/AAC.02266-17
43. Smith S, Liggitt D, Jeromsky E, Tan X, Skerrett SJ, Wilson CB. Local role for tumor necrosis factor alpha in the pulmonary inflammatory response to *Mycobacterium tuberculosis* infection. *Infect Immun*. (2002) 70:2082–9. doi: 10.1128/IAI.70.4.2082-2089.2002
44. Gill WP, Harik NS, Whiddon MR, Liao RP, Mittler JE, Sherman DR. A replication clock for *Mycobacterium tuberculosis*. *Nat Med*. (2009) 15:211–4. doi: 10.1038/nm.1915
45. McDaniel MM, Krishna N, Handagama WG, Eda S, Ganusov VV. Quantifying limits on replication, death, and quiescence of mycobacterium tuberculosis in mice. *Front Microbiol*. (2016) 7:862. doi: 10.3389/fmicb.2016.00862
46. Munoz-Elias EJ, Timm J, Botha T, Chan WT, Gomez JE, McKinney JD. Replication dynamics of *Mycobacterium tuberculosis* in chronically infected mice. *Infect Immun*. (2005) 73:546–51. doi: 10.1128/IAI.73.1.546-551.2005
47. Wynn EA, Dide-Agossou C, Reichlen M, Rossmassler K, Al Mubarak R, Reid JJ, et al. Transcriptional adaptation of *Mycobacterium tuberculosis* that survives prolonged multi-drug treatment in mice. *mBio*. (2023) 14:e0236323. doi: 10.1128/mbio.02363-23
48. McCaffrey EF, Donato M, Keren L, Chen Z, Delmastro A, Fitzpatrick MB, et al. The immunoregulatory landscape of human tuberculosis granulomas. *Nat Immunol*. (2022) 23:318–29. doi: 10.1038/s41590-021-01121-x